Journal of Materials Chemistry A

ROYAL SOCIETY OF CHEMISTRY

PAPER

View Article Online
View Journal | View Issue

Cite this: J. Mater. Chem. A, 2024, 12, 20129

Dual design of electrodes and electrolytes ensures flexible symmetric micro-supercapacitors with high energy density†

Zhiqian Cao, *[a] Jingzhi Tao[a] and Yudong Wu*[b]

According to the energy density equation $E = 0.5CV^2$, the energy density of aqueous symmetric micro-supercapacitors (AS-MSCs) can be significantly improved by increasing the working voltage of AS-MSCs. However, it is still challenging for the working voltage of AS-MSCs to break through the decomposition voltage of water (1.23 V). Herein, a flexible AS-MSCs device is assembled *via in situ* reconstructed zero-valence Ag on MXene nanosheets (ZV-AgNP-MXene) as film electrodes and utilizing polyacrylamide (PAM)/Na_2SO_4 hydrogel electrolyte. Gaining the choice of a neutral Na_2SO_4 electrolyte, the voltage of water decomposition (1.23 V) was suppressed, enabling the AS-MSC device to achieve an operation voltage output of 1.6 V. Meanwhile, *in situ* reconstruction of Ag nanoparticles as the conducting intercalator can alleviate the dense stacking of 2D MXene, providing fast ion and electron transport. Benefiting from the dual design of electrodes and electrolytes, the assembled flexible AS-MSC device achieves wide operation voltage window (1.6 V), high areal capacitance (151 mF cm^{-2}) and landmark areal energy density (52 μW h cm^{-2}). This study provides a simple and efficient strategy to increase the operating voltage and energy density of MXene-based AS-MSCs.

Received 31st March 2024
Accepted 27th June 2024

DOI: 10.1039/d4ta02145b

rsc.li/materials-a

Introduction

The rapid development of flexible microelectronics, micro-robots, implantable medical monitoring sensors and wearable electronic devices driven by micro energy storage devices has made human life smarter and more convenient in recent years.[1–3] Meanwhile, the safety of implantable and wearable microelectronic devices is crucial as they are in close contact with the human body. This has greatly stimulated the research enthusiasm of researchers for highly secure micro energy storage devices. In particular, micro energy storage devices with high safety, and high area energy/power density, originating from the integration of micro energy storage devices with microelectronic devices, are subject to strict size limitations.[4–6] In principle, the total area size of micro energy storage devices can only be at the square centimetre level or even square millimetre level.[7,8] However, current power supplies are heavy in mass, large in size, and lack flexibility to meet the demand for compatibility with flexible microelectronic devices. Therefore, the development of micro energy storage devices with high safety, high area energy/power density, low cost and integration is of great practical significance to achieve the rapid development of the smart microelectronics industry. It is well known that aqueous symmetric micro-supercapacitors (AS-MSCs) with high power density, fast charging and discharging capabilities, and excellent cycle life, have attracted great research interest as promising integrated micro power sources in microelectronics.[9–12] However, when AS-MSCs are used as micro power sources in microelectronics, they remain challenging due to their small operating voltage window (<1.23 V) and poor energy output (<10 μW h cm^{-2}).

According to the charge storage mechanism, the energy density (E) of MSCs essentially depends on the operating voltage window and the capacitance (C) as illustrated by $E = 0.5CV^2$.[13,14] Therefore, both improving the capacitance of the electrode material and enlarging the operating voltage of the device can be used to increase the energy density of MSCs. However, the conventional capacitor-type electrode materials led to the bottlenecks of low areal energy density and small operating voltage windows, which significantly hindered their commercial applications.[15–17] This urgently requires the development of novel electrode materials to improve the energy density of MSCs for practical applications. Recently, two-dimensional (2D) transition metal carbonitrides/nitrides (MXenes), as an emerging family of capacitor-type electrode materials with high volumetric capacitance (1500 F cm^{-3}), metal-level conductivity (6500 S cm^{-1}) and unique multi-layered structure, have shown encouraging promise in boosting the charge storage capacity of

[a]Key Laboratory of Green and Precise Synthetic Chemistry and Applications, Ministry of Education, School of Chemistry and Materials Science, Huaibei Normal University, Huaibei, P. R. China. E-mail: zhiqiancao@163.com

[b]Key Laboratory of Structure and Functional Regulation of Hybrid Materials, Ministry of Education, School of Materials Science and Engineering, Anhui University, Hefei 230601, P. R. China. E-mail: yudongwu94@163.com

† Electronic supplementary information (ESI) available. See DOI: https://doi.org/10.1039/d4ta02145b

the constructed energy storage devices.[18–22] It is unfortunate that when the MXene electrode material is paired with an aqueous electrolyte to assemble a symmetric MSC device, the operating voltage window of the device is only located at 0–1 V, which severely limits the energy density of the device.[23–25] Because of the easy decomposition of water molecules caused at 1.23 V, asymmetric aqueous MXene-based MSCs were designed to increase the operating voltage. Obviously, the reported asymmetric MXene-based MSCs usually have voltages lower than 1.6 V and also have some inherent drawbacks, such as a complicated preparation process and matching due to the different electrochemical behaviours between positive and negative electrodes.[26–28] In order to avoid these problems, many researchers have used the simple strategy of preparing high concentrations of salt in water (water-in-salt electrolytes) to enhance the electrochemical stability of aqueous electrolytes at high voltages (>2 V).[29,30] The water-in-salt electrolytes have high cost, poor ion transport kinetics, and poor multiplicative capacitance of the capacitor despite high voltage. Thus, the development of aqueous symmetric MSCs with high operating voltage and high energy density remains critical and challenging.

Herein, a flexible AS-MSC device is proposed *via in situ* reconstructed zero-valence Ag nanoparticles on MXene nanosheets (ZV-AgNP-MXene) as film electrodes and utilizing polyacrylamide (PAM)/Na_2SO_4 hydrogel electrolyte. Gaining the choice of a neutral Na_2SO_4 electrolyte, the voltage of water decomposition (1.23 V) was suppressed, enabling the AS-MSCs to achieve an operation voltage output of 1.6 V. Meanwhile, *in situ* reconstruction of Ag nanoparticles as the conducting intercalator can alleviate the dense stacking of 2D MXene, providing fast ion and electron transport. Benefiting from the dual design of electrodes and electrolytes, the assembled flexible AS-MSC device achieves a wide operation voltage window (1.6 V), high areal capacitance (151 mF cm^{-2}) and landmark areal energy density (52 μW h cm^{-2}). This study provides a simple and efficient strategy to increase the operating voltage and energy density of MXene-based AS-MSCs.

Results and discussion

Matching design of electrolytes–electrodes

MXene film electrodes were prepared by vacuum filtration self-assembly, as depicted in Fig. 1a. The used 2D MXene

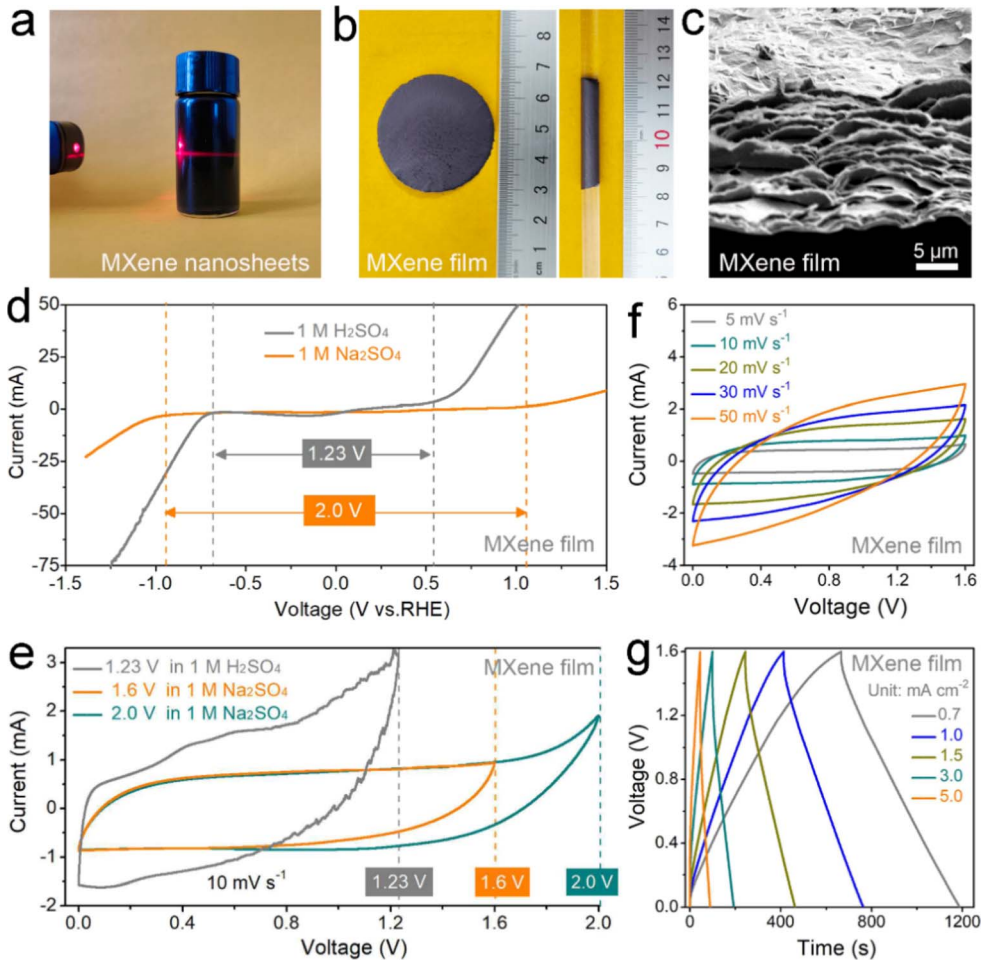

Fig. 1 (a) Photograph of the colloidal solution containing MXene nanosheets. (b) Photograph and (c) corresponding cross-sectional SEM image of the as-prepared MXene film. (d) LSV profiles and (e) CV curves of the MXene film in 1 M Na_2SO_4 and 1 M H_2SO_4. (f) CV curves and (g) corresponding GCD profiles of the AS-MSCs based on MXene film electrodes in PAM/1 M Na_2SO_4.

nanosheets were prepared by a liquid-phase exfoliation method according to our previous reports.[13,15] Multi-layer MXene was achieved through an etching process using a mixture of LiF and HCl by using Ti_3AlC_2 as the MAX precursor. After ultrasonic peeling treatment in an ice bath followed by centrifugation, 2D MXene nanosheets were achieved. The surface chemistry of MXene sheets was further investigated using X-ray photoelectron spectroscopy (XPS). The elements of Ti, C, O, F and Cl were detected in the survey spectra of MXene–$Ti_3C_2T_x$ (T represents O, OH, F, Cl and other surface terminations and x represents their corresponding number), as shown in Fig. S1.† In addition, the prepared MXene film electrodes have good flexibility, as shown in Fig. 1b. MXene's SEM directly shows that the electrode exhibits a layered structure, which facilitates the transport of ions (Fig. 1c). To expand the voltage window of MXene electrodes, it is crucial to match the electrolyte reasonably. We chose the MXene film electrode as the working electrode, a graphite rod as the counter electrode, and a Ag/AgCl electrode as the reference electrode, which together form a three-electrode test system. The electrochemical stability windows of the MXene film electrodes in 1 M H_2SO_4 and 1 M Na_2SO_4 electrolytes were determined by linear scanning voltammetry (LSV) tests in a three-electrode test system. The LSV results (Fig. 1d) showed that the electrochemical stable windows of the MXene film electrodes in 1 M H_2SO_4 and 1 M Na_2SO_4 electrolytes were 1.23 V and 2.0 V, respectively. AS-MSCs were further assembled using MXene film electrodes and polyacrylamide/1 M Na_2SO_4 (PAM/1 M Na_2SO_4 or PAM/1 M H_2SO_4) hydrogel electrolytes. Cyclic voltammetry (CV) tests were performed to evaluate the maximum operating voltage window of the assembled AS-MSCs. Fig. 1e shows the CV curves of AS-MSCs using PAM/1 M Na_2SO_4 and PAM/1 M H_2SO_4 electrolytes. All CV curves are rectangle-like, but there is a jump at the right end of the curves. However, the difference is that the AS-MSCs assembled with PAM/1 M H_2SO_4 electrolyte show a sharp jump in the CV curve before the voltage approaches 1.23 V. In contrast, the AS-MSCs prepared with PAM/1 M Na_2SO_4 electrolyte only exhibit weak transitions in the CV curve when the voltage approaches 2.0 V. As expected, the AS-MSC device assembled by employing the MXene film electrode to PAM/1 M Na_2SO_4 hydrogel electrolyte can achieve 1.6 V stable operating voltage output (Fig. 1f and g).

Structure design of flexible film electrodes

The structure design of flexible film electrodes was achieved by *in situ* reconstruction of zero-valence Ag nanoparticles on 2D MXene nanosheets (ZV-AgNP-MXene). The ZV-AgNP-MXene film was obtained *via* efficient self-reduction of $AgNO_3$ as shown in Fig. 2a. The surface of 2D MXene sheets prepared with the liquid phase etching method is terminated by abundant oxygen-containing functional groups (*e.g.* –O and –OH). The rich oxygen-containing functional groups with negative charge can physically adsorb Ag^+ from $AgNO_3$, while the Ti atoms in MXene–$Ti_3C_2T_x$ can *in situ* reduce monovalence Ag^+ to zero-valence Ag. Fig. 2b shows the uniform dispersion of tiny Ag nanoparticles on MXene nanosheets. The lattice spacing in the HR-TEM image is 0.235 nm (Fig. S2†), which corresponds to the Ag (111) reflection of the Ag nanoparticles and more accurately indicates that zero-valence Ag nanoparticles have been successfully achieved. Remarkably, the corresponding elemental mapping images (Fig. 2c) show a uniform distribution of silver signals throughout the entire Ag nanoparticles, indicating the successful synthesis of zero-valence Ag nanoparticles.

X-ray diffraction (XRD) was used to further study the existence of *in situ* reconstructed zero-valence Ag nanoparticles on MXene nanosheets (Fig. 2e). Specifically, the characteristic peak of (002) corresponds to MXene, confirming its presence as the base material within the ZV-AgNP-MXene film. Notably, the characteristic (002) peak of the ZV-AgNP-MXene film is significantly shifted to the left, which directly indicates that *in situ* reconstructed zero-valence Ag nanoparticles can widen the interlayer spacing of MXene sheets and facilitate the rapid diffusion of ions. Meanwhile, the appearance of new characteristic peaks at around 38° and 44° is attributed to the Ag (111) and (200) reflections of the ZV-AgNP-MXene film.

X-ray photoelectron spectroscopy (XPS) shows Ag 2d, Ti 2p, O 1s, C 1s and F 1s peaks belonging to the ZV-AgNP-MXene film (Fig. S3†). As shown in Fig. 2f, the peaks of Ag $3d_{5/2}$ and Ag $3d_{3/2}$ are located at 367.2 eV and 372.8 eV, respectively, which directly proves the successful synthesis of zero-valence Ag on MXene nanosheets, in agreement with the XRD results. Meanwhile, the high resolution XPS spectra of Ti 2p with the TiO_2 peak at 457.8 eV (Fig. S4†) suggested that TiO_2 was formed by oxidation during the self-reduction process of $AgNO_3$. However, the small amount of TiO_2 formed on the MXene sheets did not affect the conductivity of the ZV-Ag-NP-MXene film. Furthermore, the C–Ti (281.1 eV) and C–C (283.8 eV) bonds in the high-resolution XPS spectra of C 1s (Fig. S5†), demonstrated the well-preserved structure of MXene. In addition, the peaks located at 528.6 eV, 529.6 eV and 531.6 eV in the O 1s spectra belong to Ti–O, C–Ti–OH and C–O bonds (Fig. S6†), respectively, suggesting that many functional groups still exist in the ZV-AgNP-MXene film. Notably, the ZV-AgNP-MXene film was prepared by simple vacuum filtration of the colloidal solution containing Ag nanoparticles on MXene nanosheets (Fig. S7†). As illustrated in Fig. 2d, the prepared ZV-AgNP-MXene films exhibit good flexibility, which is favourable for their wide application in flexible supercapacitors. In addition, highly conductive zero-valence Ag nanoparticles can construct conductive pathways between the MXene sheets to improve the interlayer conductivity and charge storage capacity of the ZV-AgNP-MXene film.

Performance study of flexible devices

The AS-MSCs based on interdigital shaped electrodes and coated with PAM/Na_2SO_4 hydrogel electrolyte are designed. The total area of the interdigital shaped electrodes was about 0.68 cm^2, as illustrated in Fig. 3a. The electrochemical performance of the fabricated AS-MSC devices was methodically analysed by CV, galvanostatic charge–discharge (GCD), and electrochemical impedance spectroscopy (EIS) measurements. It is clear that the AS-MSCs based on ZV-AgNP-MXene electrodes have excellent electrochemical performance relative to the AS-MSCs based on MXene electrodes with the same content of MXene nanosheets. Concretely, the recorded CV curves from AS-MSCs based on ZV-

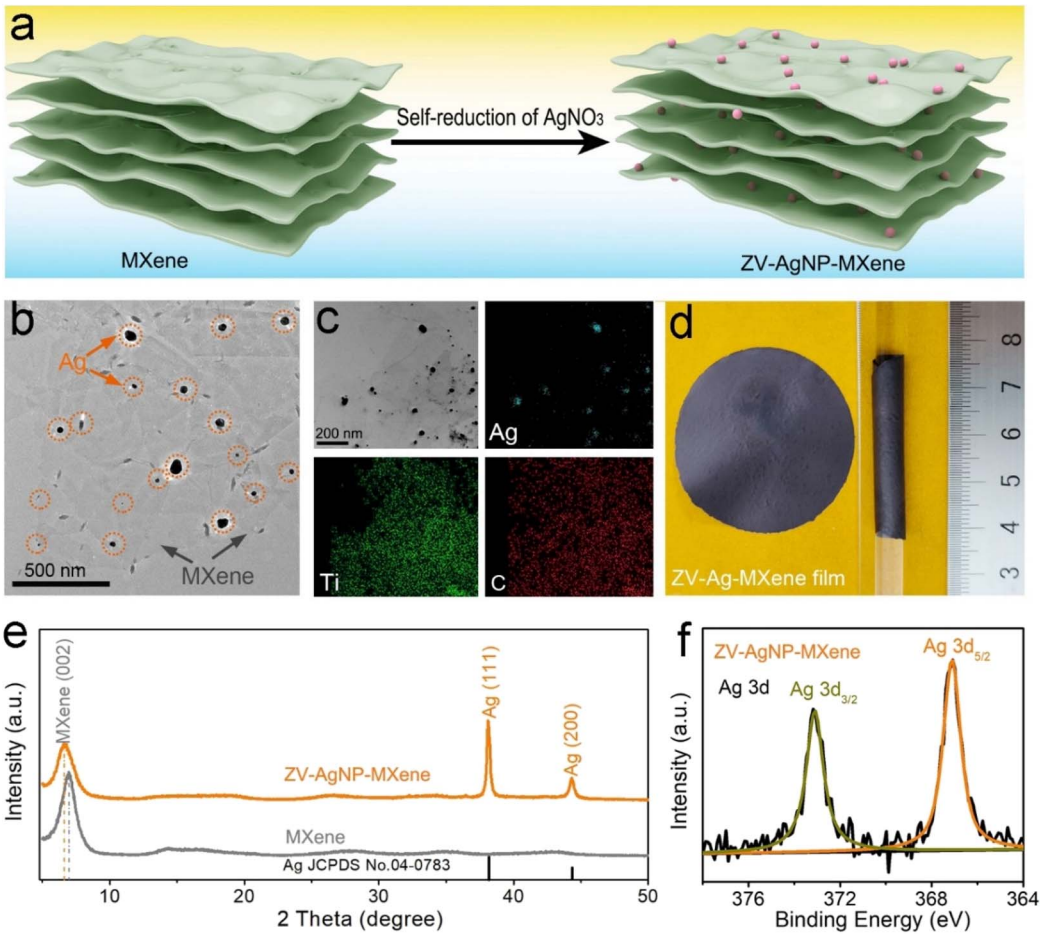

Fig. 2 (a) Schematic diagram of the self-reduction of $AgNO_3$ on MXene nanosheets. (b) TEM image and (c) EDS mapping of ZV-AgNP-MXene nanosheets. (d) Photograph of the ZV-AgNP-MXene film. (e) XRD patterns of the MXene film and ZV-AgNP-MXene film. (f) High-resolution XPS spectra of Ag 3d of the ZV-AgNP-MXene film.

AgNP-MXene electrodes showed larger integration areas and higher current intensities compared to AS-MSCs based on MXene electrodes at the same scanning speed of 10 mV s^{-1} (Fig. 3b and S8†). Meanwhile, in the corresponding GCD profiles, the AS-MSCs based on ZV-AgNP-MXene electrodes provided a longer run time than the AS-MSCs based on MXene electrodes at the same discharge current density (Fig. 3c). Therefore, at the current density of 0.7 mA cm^{-2}, the areal capacitance of the AS-MSCs based on ZV-AgNP-MXene electrodes reached 151 mF cm^{-2}, which was higher than the areal capacitance of the AS-MSCs based on MXene electrodes (117 mF cm^{-2}, Fig. 3d). In addition, when increasing the content of Ag nanoparticles (28%), the highly loaded ZV-AgNP-MXene (HD-ZV-AgNP-MXene) film electrode produced higher areal capacitance at low current density (162 mF cm^{-2} at 0.7 mA cm^{-2}, Fig. S9 and S10†), which originated from the fact that more Ag nanoparticles enlarged the layer spacing of MXene sheets and stored more ions. However, the HD-ZV-AgNP-MXene film electrode had a lower rate capability performance (65.4%) compared to the ZV-AgNP-MXene film electrode (78.1%, Fig. S10†). Thus, the ZV-AgNP-MXene film electrode is more suitable for application as an electrode for flexible devices.

To investigate the storage mechanism of the electrodes, *in situ* Raman spectroscopy was further employed to check the changes in the positive and negative electrodes of the device during charging and discharging (Fig. 3e). Initially, a clear Raman characteristic peak at ~727 cm^{-1} representing the out-of-plane vibration of the C atom in the Ti_3C_2═O functional group was observed in both the positive and negative electrodes (Fig. 3f and g). Notably, in the negative pole, the peak is gradually shifted to a lower wave number, accompanied by a decrease in intensity. In contrast, in the positive electrode, there is no change in the wave number of the peak except for a slight weakening of the intensity. This is due to the gradual replacement of the MXene–Ti_3C_2═O species by the newly formed MXene–Ti_3C_2–O–Na species within the negative electrode during charging based on the inserted Na^+, with the opposite phenomenon observed during discharge. In contrast, during charging/discharging, adsorption/desorption of SO_4^{2-} is predominant in the positive electrode, with no chemical bonding to MXene–Ti_3C_2═O.

The link between the structural design of the used film electrodes and the improved areal capacitance can be further elucidated by EIS tests (Fig. 3h). The Nyquist plots show a high-frequency region associated with ohmic resistance (R_e) and

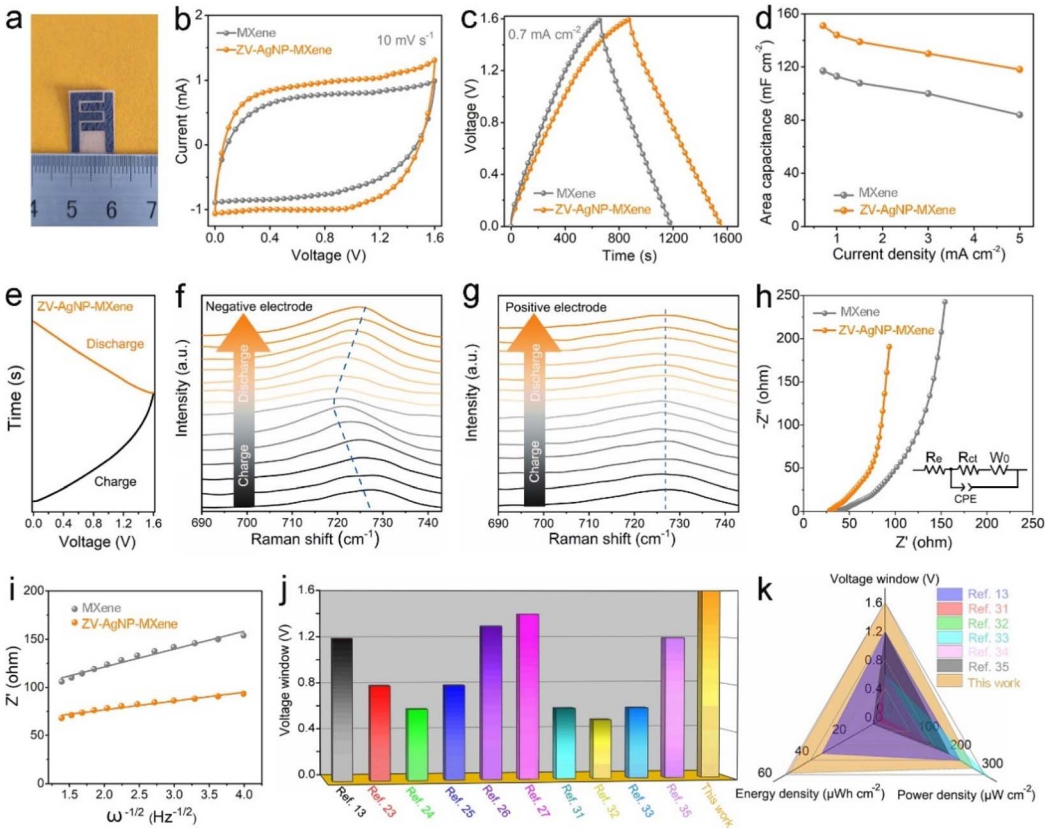

Fig. 3 (a) Photograph of AS-MSCs based on ZV-AgNP-MXene film electrodes. (b) CV curves, (c) GCD profiles and (d) corresponding areal capacitance of AS-MSCs based on MXene and ZV-AgNP-MXene film electrodes. *In situ* Raman spectroscopy of (f) negative electrode and (g) positive electrode of the AS-MSCs during the (e) charging/discharging process. (h) Nyquist plots and (i) plots of Z' against $\omega^{-1/2}$ comparison of AS-MSCs based on MXene and ZV-AgNP-MXene film electrodes. (j) The operating voltage comparison and (k) performance parameter comparison of MSCs based on MXene-based film electrodes.

charge transfer resistance (R_{ct}) at the electrode/electrolyte interface, and straight lines in the low-frequency regions correspond to the Warburg impedance (W_0) attributed to ion diffusion through the electrode material, respectively. It is obvious that ZV-AgNP-MXene film electrodes (28 Ω) exhibit a smaller ohmic resistance compared to MXene film electrodes (39 Ω). Moreover, a smaller Warburg factor (σ, the slope of Z' against $\omega^{-1/2}$) represents faster ion diffusion kinetics, which is also beneficial for improving the charge storage capacity of the film electrodes. According to calculations, the Warburg coefficient of ZV-AgNP-MXene film electrodes is 9.2, which is much smaller than that of the MXene film electrodes (18.6, Fig. 3i), resulting in a significant increase in areal capacitance for the AS-MSCs based on ZV-AgNP-MXene film electrodes. Therefore, *in situ* reconstruction of highly conductive Ag nanoparticles on MXene nanosheets not only significantly improves the electron migration efficiency, but also facilitates the rapid diffusion of ions, thereby increasing the charge storage capacity of the ZV-AgNP-MXene electrodes. Additionally, the ZV-AgNP-MXene film electrode was employed with a neutral electrolyte (Na_2SO_4), enabling the assembled AS-MSC devices to achieve an operating voltage output of 1.6 V, which is highly advantageous among the currently reported aqueous asymmetric/symmetric MXene-based MSCs (Fig. 3j). According to the energy density equation $E = 0.5CV^2$, the energy density of aqueous MSCs can be significantly improved by increasing the working voltage of MSCs. Consequently, the energy density of AS-MSC devices using ZV-AgNP-MXene film electrodes is highly competitive (up to 52 μW h cm^{-2} at 0.7 mA cm^{-2}) relative to the currently reported MSCs based on MXene film electrodes (Fig. 3k).[13,31–35]

Recently, flexible microelectronics, implantable medical monitoring sensors, and wearable electronics require compatible micro-energy-storage-devices that maintain a stable electrochemical performance output under various mechanical deformations.[36–45] Benefiting from the excellent electrochemical performance of a single AS-MSC device, we further designed and assembled a novel flexible AS-MSC device, as illustrated in Fig. 4a. The detailed preparation steps of the flexible AS-MSC device are described in the Experimental section of the ESI.† The fabricated flexible AS-MSC device consists of three AS-MSC units connected in series *via* copper leads, as shown in Fig. 4b. Moreover, Fig. 4c and d show that the novel flexible AS-MSC device consisting of 3 series-connected AS-MSCs can output 4.8 V, directly illustrating its great potential in practical micro energy storage devices. Notably, the flexible device consisting of three AS-MSC devices connected in parallel can output larger current and higher energy, as depicted in Fig. S11 and S12.† Furthermore, the fabricated flexible AS-MSC device based on

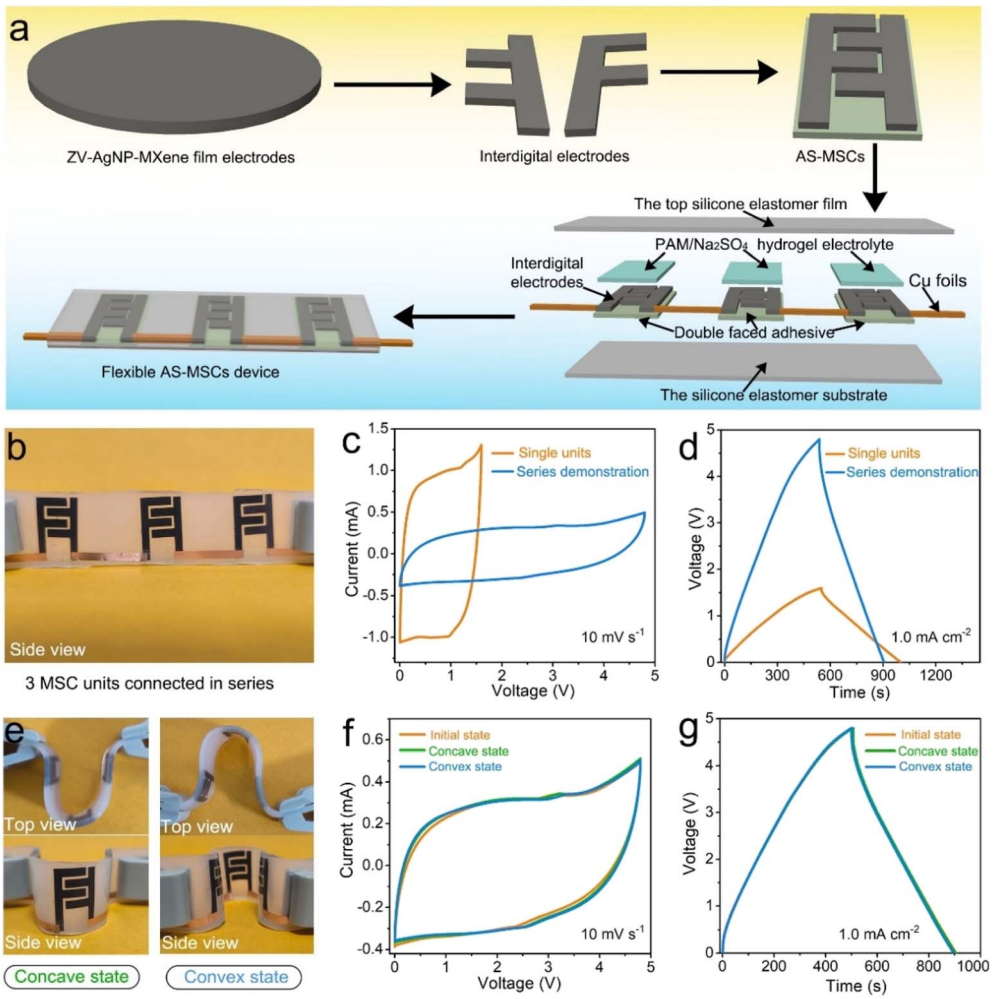

Fig. 4 (a) The fabrication schematic of the flexible AS-MSC devices. (b) Photographs, (c) CV curves, and (d) GCD profiles of a single AS-MSC unit and series-connected AS-MSC devices. (e) Photographs, (f) CV curves and (g) GCD profiles of the series-connected AS-MSC devices in the initial state, concave state, and convex state.

ZV-AgNP-MXene film electrodes exhibited 60% capacity retention (at a high current density of 5.0 mA cm^{-2}) after 3000 cycles in the 0–4.8 V operating voltage window (Fig. S13†). Fig. 4e shows photographs of flexible AS-MSC devices in concave and convex states. In addition, the CV curves and GCD profiles remained consistent under different bending states, indicating that the good structural design of ZV-AgNP-MXene film electrodes effectively ensured the stability of the electrochemical output (Fig. 4f and g). Consequently, the experimental results fully confirm the rationality and effectiveness of the flexible AS-MSC device based on ZV-AgNP-MXene film electrodes, further enhancing the competitiveness of flexible MSCs to support the burgeoning wearable/implantable microelectronics.

Conclusions

In summary, a flexible AS-MSC device is reported *via in situ* reconstructed zero-valence Ag nanoparticles on MXene nanosheets (ZV-AgNP-MXene) as film electrodes and utilizing polyacrylamide (PAM)/Na_2SO_4 hydrogel electrolyte. Gaining the choice of a neutral Na_2SO_4 electrolyte, the voltage of water decomposition (1.23 V) was suppressed, enabling the AS-MSC device to achieve an operation voltage output of 1.6 V. More remarkably, *in situ* reconstruction of Ag nanoparticles as the conducting intercalator can alleviate the dense stacking of 2D MXene, providing fast ion and electron transport. In addition, the dual design of electrodes and electrolytes ensures that the assembled flexible symmetric micro-supercapacitor achieves a stable output with high operation voltage, high areal capacitance and high energy density. This study provides a simple and efficient strategy to increase the operation voltage and energy density of MXene-based symmetric supercapacitors.

Data availability

All relevant data are within the manuscript and its additional files.

Conflicts of interest

There are no conflicts to declare.

Acknowledgements

This work was financed by the Key Natural Science Research Project of Anhui Provincial Education Department (2022AH050405), Independent Research Project of Key Laboratory of Green and Precise Synthetic Chemistry and Applications (Huaibei Normal University), Ministry of Education (KLGPSCA202402), and 2024 Anhui Province College Student Innovation and Entrepreneurship Training Program Project.

Notes and references

1 A. K. Katiyar, A. T. Hoang, D. Xu, J. Hong, B. J. Kim, S. Ji and J.-H. Ahn, *Chem. Rev.*, 2024, **124**, 318–419.
2 Z. Y. Hui, L. R. Zhang, G. Z. Ren, G. Z. Sun, H.-D. Yu and W. Huang, *Adv. Mater.*, 2023, **35**, 2211202.
3 P. P. Zhang, S. Yang, H. G. Xie, Y. Li, F. X. Wang, M. M. Gao, K. Guo, R. H. Wang and X. Lu, *ACS Nano*, 2022, **16**, 17593–17612.
4 X. Wang and Z.-S. Wu, *EcoMat*, 2020, **2**, e12042.
5 X. L. Pan, X. F. Hong, L. Xu, Y. X. Li, M. Y. Yan and L. Q. Mai, *Nano Today*, 2019, **28**, 100764.
6 W. Q. Wang, L. Gao, Z. M. Kong, B. C. Ma, M. Y. Han, G. C. Wang and C. Z. Li, *Adv. Mater.*, 2023, **35**, 2303353.
7 S. S. Bi, H. M. Cao, R. Wang, F. Wan and Z. Q. Niu, *J. Energy Chem.*, 2021, **63**, 25–39.
8 Z. Yan, S. J. Luo, Q. Li, Z.-S. Wu and S. Z. Liu, *Adv. Sci.*, 2024, **11**, 2302172.
9 H. L. Liu, Z. J. Sun, Y. Chen, W. J. Zhang, X. Chen and C.-P. Wong, *ACS Nano*, 2022, **16**, 10088–10129.
10 J. Q. Qin, H. T. Zhang, Z. Yang, X. Wang, P. Das, F. Zhou and Z.-S. Wu, *J. Energy Chem.*, 2023, **81**, 410–431.
11 L. Li, J. Meng, X. R. Bao, Y. P. Huang, X.-P. Yan, H.-L. Qian, C. Zhang and T. X. Liu, *Adv. Energy Mater.*, 2023, **13**, 2203683.
12 H. B. Hu and T. Hua, *J. Mater. Chem. A*, 2017, **5**, 19639–19648.
13 Z. Q. Cao, J. M. Fu, M. Z. Wu, T. Hua and H. B. Hu, *Energy Storage Mater.*, 2021, **40**, 10–21.
14 Y. J. Li, T. Liu, Y. P. Liu, F. B. Meng and Z. Q. Cao, *Chem. Eng. J.*, 2024, **479**, 147906.
15 Z. Q. Cao, G. J. Liang, D. Ho, C. Y. Zhi and H. B. Hu, *Adv. Funct. Mater.*, 2023, **33**, 2303060.
16 P. P. Zhang, Y. Li, G. Wang, F. X. Wang, S. Yang, F. Zhu, X. D. Zhuang, O. G. Schmidt and X. L. Feng, *Adv. Mater.*, 2019, **31**, 1806005.
17 H. Wang, J. M. Li, X. X. Kuai, L. M. Bu, L. J. Gao, X. Xiao and Y. Gogotsi, *Adv. Energy Mater.*, 2020, **10**, 2001411.
18 A. VahidMohammadi, J. Rosen and Y. Gogotsi, *Science*, 2021, **372**, 1165.
19 M. J. Wang, Y. F. Cheng, H. Y. Zhang, F. Cheng, Y. X. Wang, T. Huang, Z. C. Wei, Y. H. Zhang, B. H. Ge, Y. N. Ma, Y. Yue and Y. H. Gao, *Adv. Funct. Mater.*, 2023, **33**, 2211199.
20 Z. F. Zhao, S. Wang, F. Wan, Z. W. Tie and Z. Q. Niu, *Adv. Funct. Mater.*, 2021, **31**, 2101302.
21 Y. Y. Zhu, S. Wang, J. X. Ma, P. Das, S. H. Zheng and Z.-S. Wu, *Energy Storage Mater.*, 2022, **51**, 500–526.
22 S. Abdolhosseinzadeh, R. Schneider, A. Verma, J. Heier, F. Nüesch and C. F. Zhang, *Adv. Mater.*, 2020, **32**, 2000716.
23 G. Y. Zhu, Y. N. Hou, J. Q. Lu, H. C. Zhang, Z. C. Zhuang, M. M. Baig, M. Z. Khan, M. A. Akram, S. Y. Dong, P. Liu, X. L. Ge and Y. Z. Zhang, *J. Mater. Chem. A*, 2023, **11**, 25422–25428.
24 Y. D. Wu, H. B. Hu, C. Z. Yuan, J. Song and M. Z. Wu, *Nano Energy*, 2020, **74**, 104812.
25 M. M. Yuan, L. B. Wang, X. Q. Liu, X. Y. Du, G. B. Zhang, Y. K. Chang, Q. X. Xia, Q. K. Hu and A. G. Zhou, *Chem. Eng. J.*, 2023, **451**, 138686.
26 H. R. Wang, C.-F. Du, Y. Q. Xue, X. Song, S. L. Lei, Z. W. Ren, R. S. Guo, H. Yu and F. Zhou, *J. Mater. Chem. A*, 2022, **10**, 20953–20963.
27 Q. Yang, Z. D. Huang, X. L. Li, Z. X. Liu, H. F. Li, G. J. Liang, D. H. Wang, Q. Huang, S. J. Zhang, S. M. Chen and C. Y. Zhi, *ACS Nano*, 2019, **13**, 8275–8283.
28 Z. Li, J. Song, H. B. Hu, C. Z. Yuan, M. Z. Wu and D. Ho, *J. Mater. Chem. A*, 2021, **9**, 2899–2911.
29 H. Avireddy, B. W. Byles, D. P. Galindo, J. J. Biendicho, X. H. Wang, C. Flox, O. Crosnier, T. Brousse, E. Pomerantseva, J. R. Morante and Y. Gogotsi, *Nano Energy*, 2019, **64**, 103961.
30 Y. H. Shen, B. Liu, X. R. Liu, J. Liu, J. Ding, C. Zhong and W. B. Hu, *Energy Storage Mater.*, 2021, **34**, 461–474.
31 S. Li, Q. Shi, Y. Li, J. Yang, T.-H. Chang, J. W. Jiang and P.-Y. Chen, *Adv. Funct. Mater.*, 2020, **30**, 2003721.
32 C. F. Zhang, L. McKeon, M. P. Kremer, S.-H. Park, O. Ronan, A. Seral-Ascaso, S. Barwich, C. Ó Coileáin, N. McEvoy, H. C. Nerl, B. Anasori, J. N. Coleman, Y. Gogotsi and V. Nicolosi, *Nat. Commun.*, 2019, **10**, 1795.
33 C. F. Zhang, M. P. Kremer, A. Seral-Ascaso, S.-H. Park, N. McEvoy, B. Anasori, Y. Gogotsi and V. Nicolosi, *Adv. Funct. Mater.*, 2018, **28**, 1705506.
34 S. Q. Jiao, A. G. Zhou, M. Z. Wu and H. B. Hu, *Adv. Sci.*, 2019, **6**, 1900529.
35 X. X. Li, Y. N. Ma, P. Z. Shen, C. K. Zhang, M. L. Cao, S. J. Xiao, J. F. Yan, S. J. Luo and Y. H. Gao, *Adv. Mater. Technol.*, 2020, **5**, 2000272.
36 H. F. Li, Z. J. Tang, Z. X. Liu and C. Y. Zhi, *Joule*, 2019, **3**, 613–619.
37 X. L. Zhu, Y. Zhang, Z. M. Man, W. Y. Lu, W. Chen, J. H. Xu, N. Z. Bao, W. X. Chen and G. Wu, *Adv. Mater.*, 2023, **35**, 2307186.
38 D. H. Wang, C. P. Han, F. N. Mo, Q. Yang, Y. W. Zhao, Q. Li, G. J. Liang, B. B. Dong and C. Y. Zhi, *Energy Storage Mater.*, 2020, **28**, 264–292.
39 J. Y. He, L. Q. Cao, J. J. Cui, G. W. Fu, R. Y. Jiang, X. Xu and C. Guan, *Adv. Mater.*, 2024, **36**, 2306090.
40 Y. L. An, Y. Tian, H. T. Shen, Q. Y. Man, S. L. Xiong and J. K. Feng, *Energy Environ. Sci.*, 2023, **16**, 4191–4250.
41 M. Y. Feng, Y. Zhang, X. L. Zhu, W. X. Chen, W. Y. Lu and G. Wu, *Angew. Chem.*, 2023, **62**, e202307195.
42 G. Wu, X. J. Wu, X. L. Zhu, J. H. Xu and N. Z. Bao, *ACS Nano*, 2022, **16**, 10130–10155.

43 Z. Q. Cao, G. Y. Hu, W. X. Feng, J. Ru and Y. J. Li, *Carbon Neutralization*, 2023, **2**, 699–708.
44 X. W. Huang, X. Y. Lyu, G. H. Wu, J. Yang, R. Zhu, Y. Tang, T. T. Li, Y. J. Wang, D. Yang and A. G. Dong, *Adv. Energy Mater.*, 2023, **14**, 2303417.
45 G. Y. Zhu, Y. N. Hou, J. Q. Lu, H. C. Zhang, Z. C. Zhuang, M. M. Baig, M. Z. Khan, M. A. Akram, S. Y. Dong, P. Liu, X. L. Ge and Y. Z. Zhang, *J. Mater. Chem. A*, 2023, **11**, 25422–25428.